Engineering Fracture Mechanics 308 (2024) 110353

Contents lists available at ScienceDirect

Engineering Fracture Mechanics

journal homepage: www.elsevier.com/locate/engfracmech

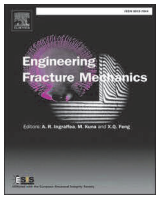

Interlaminar fracture behaviour of emerging laminated-pultruded CFRP plates for wind turbine blades

Xi Li [a,b,*], Francisco Monticeli [a], John-Alan Pascoe [a], Yasmine Mosleh [c]

[a] Department of Aerospace Structures and Materials, Faculty of Aerospace Engineering, Delft University of Technology, Kluyverweg 1, 2629 HS Delft, the Netherlands
[b] Department of Aerospace Science and Technology, Politecnico di Milano, Via La Masa 34, 20156 Milano, Italy
[c] Department of Engineering Structures, Faculty of Civil Engineering and Geosciences, Delft University of Technology, Stevinweg 1, 2628 CN Delft, the Netherlands

ARTICLE INFO

Keywords:
Crack initiation
Crack propagation
Failure criteria
Fracture toughness
Pultruded Composite

ABSTRACT

Laminated pultruded composite plates are gaining interest for use in wind turbine blades due to their excellent structural performance with affordable cost. However, there is limited understanding of their fracture properties. The present work explores the interlaminar fracture behaviour of pultruded composite plates, bonded through resin infusion, to form thick CFRP structures. Mode-I, –II, and mixed-mode (I/II) tests were performed to obtain fracture properties at different mixed-mode ratios. Mode I crack propagation exhibits stick–slip behaviour, resulting in brittle failure in a few steps, while mode II provides more stable crack propagation along with cohesive failure. The mixed-mode fracture patterns follow the trend of the mode-mix ratios, in which higher mode-mix ratios (more mode II) induce more stable crack propagation. Benzeggagh-Kenane and power law criteria were compared regarding their prediction of crack initiation toughness given a mode mix ratio, and a linear relation between the mixed-mode I/II fracture toughness components could exist at interfaces of laminated pultruded plates. Meanwhile, applicability of testing standards and the effect of manufacturing-induced defects on fracture properties are thoroughly discussed. The results show that existing standards provide sufficient support for characterising fracture properties of bonded pultruded plates; and that manufacturing-induced defects can be detrimental to crack propagation and cause more brittle behaviour in mode I dominant cases, while beneficial effect of defects by toughening the interface was exhibited in mode II dominant cases.

1. Introduction

Driven by the increasing demand for clean energy, pultruded carbon fibre-reinforced polymer (CFRP) plates become the emerging enablers for scaling up large wind turbine blades with affordable cost while maintaining high structural performance [1,2]. These pultruded plates have been used in spar caps to support/transfer increased loads in the flap direction [3]. To meet design requirements for thicker plates, pre-cured pultruded plates are usually bonded together using an epoxy resin system, which may create weak load-bearing or load-transferring regions threatening the structural integrity and safety of the resulting laminate [4,5]. Therefore, it is

* Corresponding author.
E-mail addresses: Xi.Li@polimi.it (X. Li), F.M.Monticeli@tudelft.nl (F. Monticeli), J.A.Pascoe@tudelft.nl (J.-A. Pascoe), Y.Mosleh@tudelft.nl (Y. Mosleh).

https://doi.org/10.1016/j.engfracmech.2024.110353
Received 12 April 2024; Received in revised form 25 June 2024; Accepted 28 July 2024
Available online 31 July 2024
0013-7944/© 2024 The Authors. Published by Elsevier Ltd. This is an open access article under the CC BY license (http://creativecommons.org/licenses/by/4.0/).

Nomenclature

Symbols	Descriptions [Units]
A^1	the slope of the least square plot of a/h as a function of $C^{1/3}$ for DCB specimens [$(N/mm)^{1/3}$]
a	crack length [mm]
a_e	effective crack length for ELS tests [mm]
a_0	intial crack length [mm]
b	specimen width [mm]
C	compliance calculated δ/P [mm/N]
c	the distance from the load line to the middle support contacting to the upper arm [mm]
c_g	centre of gravity for MMB test apparatus [mm]
c_{sys}	system compliance in the MMB apparatus [mm/N]
E_1	flexural modulus obtained the clamp calibration on the ELS test apparatus [MPa]
E_{11t}	longitudianl tensile modulus [MPa]
E_{11c}	longitudianl compressive modulus [MPa]
E_{1f}	bending modulus of the MMB specimen[MPa]
E_{22t}	transverse tensile modulus along the y direction [MPa]
E_{22c}	transverse compressvie modulus along the y direction [MPa]
E_{33}	transverse modulus along the z direction [MPa]
G_{12},G_{13}	in-plane shear modulus [MPa]
G_{23}	transverse shear modulus [MPa]
G_I	mode I SERR [J/m^2]
G_{IC}	critical mode I SERR at crack initiation [J/m^2]
G_{II}	mode II SERR [J/m^2]
G_{IIC}	critical mode II SERR at crack initiation [J/m^2]
G_T	total SERR [J/m^2]
h	half specimen thickness [mm]
L	half-span length of the MMB test apparatus [mm]
L_{free}	distance from the load line to the clamping fixture for ELS [mm]
M	mixed-mode ratio [-]
m	slope of the least square plot of C as a function of a^3 for ELS specimens [$1/(N\times mm^2)$]
m_1	slope of loading displacement curve [N/mm]
n	slope of the least square plot of $\log(C)$ as a function of $\log(a)$ for DCB specimens [log(mm/N)/ log(mm)]
P	applied load [N]
P_{est}	estimated value of critical load for MMB tests [N]
P_g	weight of lever and attached apparatus [N]
S_{11t}	longitudianl tensile strength [MPa]
S_{11c}	longitudianl compressive strength [MPa]
S_{22t}	transverse tensile strength [MPa]
S_{22c}	transverse compressvie strength [MPa]
S_{23}	in-plane shear strength [MPa]
$slop$	slope of the linear regression to the $C^{1/3}$ versus free length Lfree, obtained by the clamp calibration for ELS test apparatus [$1/(N^{1/3}\times mm^{2/3})$]
α	mode mixture transformation parameter for setting lever length [-]
β	non-dimensional crack length correction for mode mixture [-]
Δ	intercept of the least square plot of $C^{1/3}$ as a function of a for DCB specimens [mm]
Δ_{clamp}	ratio of the intercept to the slope for the linear regression to the $C^{1/3}$ versus free length L_{free} from clamp clibration for ELS specimens [mm]
δ	displacement [mm]
ν_{12}, ν_{31}	in-plane Poisson's ratio [-]
ν_{23}	transverse Poisson's ratio [-]
Γ	transverse modulus correction parameter [-]
χ	crack length correction parameter [-]

Abbreviations

CC	Compliance Calibration
CBTE	Corrected Beam Theory using Effective crack length
CFRP	Carbon Fibre Reinforced Polymer
DCB	Double Cantilever Beam
ECM	Experimental Compliance Method

ELS	End-Loaded Split
MBT	Modified Beam Theory
MCC	Modified Compliance Calibration
MMB	Mixed-Mode Bending
SBT	Simple Beam Theory
SERR	Strain Energy Release Rate
VIS	VISually observed

necessary to understand the fracture behaviours of such laminated pultruded CFRP plates under different fracture modes, and to further establish fracture criteria to generate design allowables and evaluate service life.

Diverse test configurations have been developed to characterise the interlaminar fracture toughness of composite laminates under a specific fracture mode. Some of them have been standardised, among others: the double cantilever beam test (DCB – ASTM D5528 [6]) for pure mode-I, the end-loaded split test (ELS – ISO 15114 [7]) and end-notched flexure test (ENF – ASTM D7905 [8]) for pure mode-II, and the mixed-mode bending test (MMB – ASTM D6671 [9]) for mixed-mode I/II. However, questions may arise here regarding the analysis of fracture behaviours of laminated pultruded composite plates. Should they be treated as composite laminates or adhesive joints? What influence does the mode mix ratio have on the development of the fracture pattern? Can testing standards proposed for composite laminates be applicable to measure the interlaminar fracture resistance of bonded pultruded plates? How do manufacturing-induced defects (i.e. air bubbles) at the bonding resin layer affect their interlaminar fracture properties?

Data reduction methods proposed for composite laminates in the test standards could be followed to calculate the interlaminar fracture properties of laminated-pultruded composite plates. However, they may not be suitable for the thick bond layers and composite beams [10,11]. Cintra et al. [12] concluded that the Modified Beam Theory method [6] for crack propagation in mode I presented the closest results to numerical predictions. At the same time, similar mode II fracture toughness properties can be observed from ELS tests by using the Experimental Compliance Method and Corrected Beam Theory using effective crack length [8].

However, it is unclear whether the testing configurations or specimen dimensions suggested in the standards should be modified, considering the overall thickness of these laminated-pultruded composite plates can be out of the recommended range. For instance, the thickness of specimens is advised as 3–5 mm for DCB and MMB tests, and 3 mm for ELS tests for CFRP laminates with a 60 % fibre volume fraction. Previously, some researchers have recommended modifications to the standard dimensions: Burda et al. [13] recommended to use at least 250 mm length of DCB specimens to characterise the pure mode-I and provide a suitable R-curve of pultruded glass fibre-reinforced epoxy rods. Yan et al. [14] found that mode-II crack propagation using the ENF test configuration becomes more stable when increasing pre-crack length for pultruded carbon fibre-epoxy composites. Zhang et al. [15] increased the length of ELS specimens to investigate the mode-II fracture properties for an adhesive layer of 2 mm thickness. Clearly, choosing proper specimen dimensions and pre-crack lengths that can promote crack stability and guarantee the sufficient crack propagation in desired fracture modes is necessary for laminated-pultruded composite plates [12,16], especially the very thick ones.

Additionally, defects at the bonded layer are hard to control during manufacturing, especially when applying the resin infusion process to bond the pre-cured pultruded CFRP plates. The viscosity of the resin and its mixture with the hardener is highly sensitive to the ambient environment [17]. We lack sufficient understanding of the manufacturing-induced defects on fracture behaviours of laminated pultruded composite plates, where limited work can be found in the literature. Kumar [18,19] numerically investigated the effect of randomly distributed defects on mode I and mode II interlaminar fracture of composite laminates, and reported peak load and fracture energy corresponding to delamination onset scaling with the area fraction of defects. Ranade et al. [20] found that a weak interface with well-placed artificial defects can reverse the trend of the delamination resistance curve for adhesive joints. Li et al. [21,22] systematically investigated the effect of material variability and its spatial correlation at interfaces on toughening secondary bonded composite joints, achieved by triggering different debonding phenomenology, such as crack tip transfer, crack bifurcation or

Table 1
Material properties of Zoltek™ PX35 pultruded plate with a thickness of 3 mm (Note: 1- x direction;2-y direction; 3-z direction) [23].

Material properties	Units	Values
Longitudianl tensile modulus E_{11t}	MPa	148,000
Longitudianl compressive modulus E_{11c}	MPa	136,000
Transverse tensile modulus along the y direction E_{22t}	MPa	9500
Transverse compressvie modulus along the y direction E_{22c}	MPa	11,000
Transverse modulus along the z direction E_{33}	MPa	9000
In-plane shear modulus G_{12},G_{13}	MPa	5000
Transverse shear modulus G_{23}	MPa	3300
In-plane Poisson's ratio ν_{12}, ν_{31}	–	0.263
Transverse Poisson's ratio ν_{23}	–	0.403
Longitudianl tensile strength S_{11t}	MPa	1850
Longitudianl compressive strength S_{11c}	MPa	1400
Transverse tensile strength S_{22t}	MPa	55
Transverse compressvie strength S_{22c}	MPa	160
In-plane shear strength S_{23}	MPa	55

ligament bridging. Overall, more efforts should be devoted to improving the reliability of the characterisation of fracture properties of laminated pultruded composite plates.

In this context, the main objective of the present work is to provide a comprehensive insight on quasi-static fracture behaviours of laminated pultruded composite plates under different loading modes. Furthermore, the applicability of test standards on the characterisation of fracture properties and the effect of defects on interlaminar fracture resistance is explored. Firstly, a resin infusion process was performed to bond pre-cured pultruded CFRP plates, after which DCB, ELS and MMB tests were implemented to obtain the mode I, mode II and mixed-mode I/II fracture properties for both crack initiation and crack propagation. The failure patterns of the fractured surface were identified by microscopic inspection. Eventually, different mixed-mode I/II failure criteria were compared, and the applicability of test standards and the effect of defects on characterising fracture properties were discussed.

2. Experimental methods

2.1. Materials and specimen preparation

The research target of the present work is the Zoltek^{TM} PX35 pultruded plate with a thickness of 3 mm and a width of 60 mm. The fibre volume fraction is 65 % and the fibre orientation is 0°. Table 1 lists material properties of this pultruded CFRP plate. The resin infusion process was used to bond the plates, which has previously been applied to form thick CFRP structures [14]. The resin system is SWANCOR 2511-1AL/BL. During the infusion process, a glass-fibre veil (M524-ECR30A) with an areal weight of 30 g/m^2 was placed at the interface over a length of 150–170 mm to improve the fracture toughness at interfaces, while a piece of vacuum bag material (thickness: ~0.05 mm) was inserted to create an initial cracking region with a length of 100 mm (Fig. 1 (a)). Afterwards, the panels were cured at room temperature for 24 h and then post-cured at 65°C for 3 h and at 80°C for 4 h before cooling to room temperature. For each infusion, four pultruded CFRP plates were placed together on an aluminium base plate, with another four on the top, ensuring sufficient flow of resin at the interfaces (Fig. 1 (a)). Eventually, three bonded panels with approximately 240 mm in width and 250–270 mm in length were manufactured, and they were later inspected by an ultrasonic C-scanner. In contrast to Panel A and Panel C, some debonding regions at interfaces were observed in Panel B, as shown in Fig. 1 (b). This may be attributed to inadequate degassing of mixed resin and hardener or the overflow of infused resin due to a loose valve on the resin outlet tube during the early-curing process at room temperature.

A water-cooled diamond saw was used to cut bonded panels based on the specimen design presented in Fig. 2 (a)-(c). The nominal width of DCB specimens and MMB specimens is 25 mm, while it is 20 mm for ELS specimens. Despite that specimen thickness (~6.1 mm) is out of range recommended in [6,7,9], we comply to following rules available in the test standards [6,7,9] as the guidance to determine reasonable specimen dimensions and initial crack lengths: (1) for DCB specimens, the ratio of the initial crack length to the overall thickness is kept over ten for accurate data reduction procedures [6]; (2) for ELS specimens, a ratio of initial crack length to free length L_{free} larger than 0.55 is guaranteed to promote stability of crack propagation [7,24], where the free length for ELS specimens is the distance from the load line to the front of the clamping fixture; (3) for MMB specimens, the initial length a_0 satisfies $0.45L<a_0<L-3h$ as recommended in ASTM D6671 [9], where L is the half-span length of the MMB test apparatus, and h is half the specimen thickness. As a result, the initial crack length is 80 mm for DCB specimens with a length of 200 mm. In the ISO 15114 test standard, a ratio of initial length to free length equal to 0.75 was mentioned that can guarantee the crack stability. However, this large ratio causes small space for crack propagation before reaching the clamping region. Therefore, preliminary studies were performed for ELS specimens with two initial crack lengths, i.e. 66 mm and 82.5 mm, both of which have the same free length 110 mm (Fig. 2 (b)). The

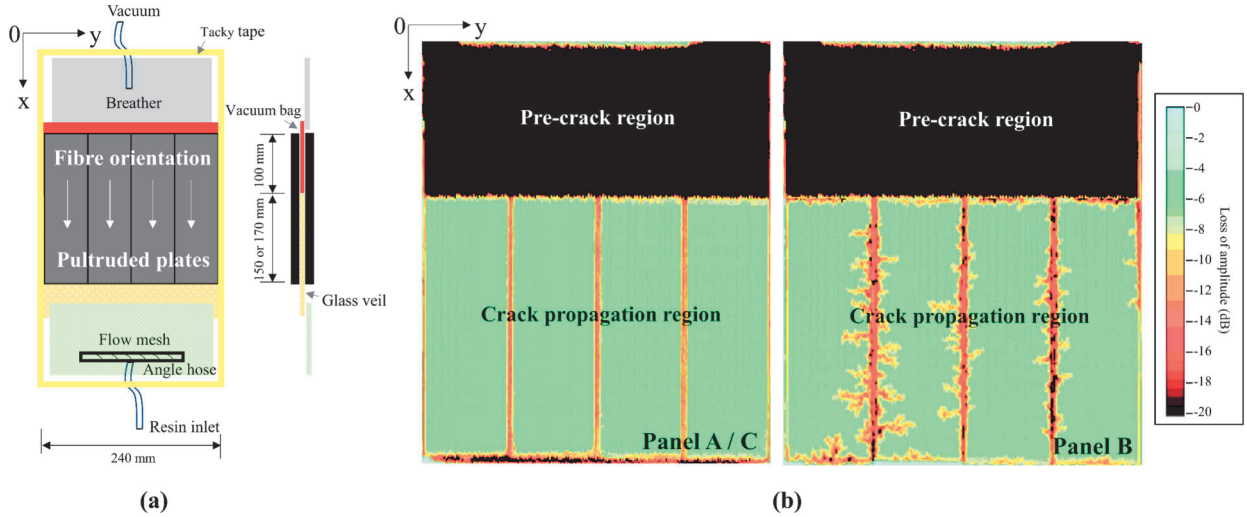

Fig. 1. Resin-infusion system (a); C-scan results of three bonded panels (b).

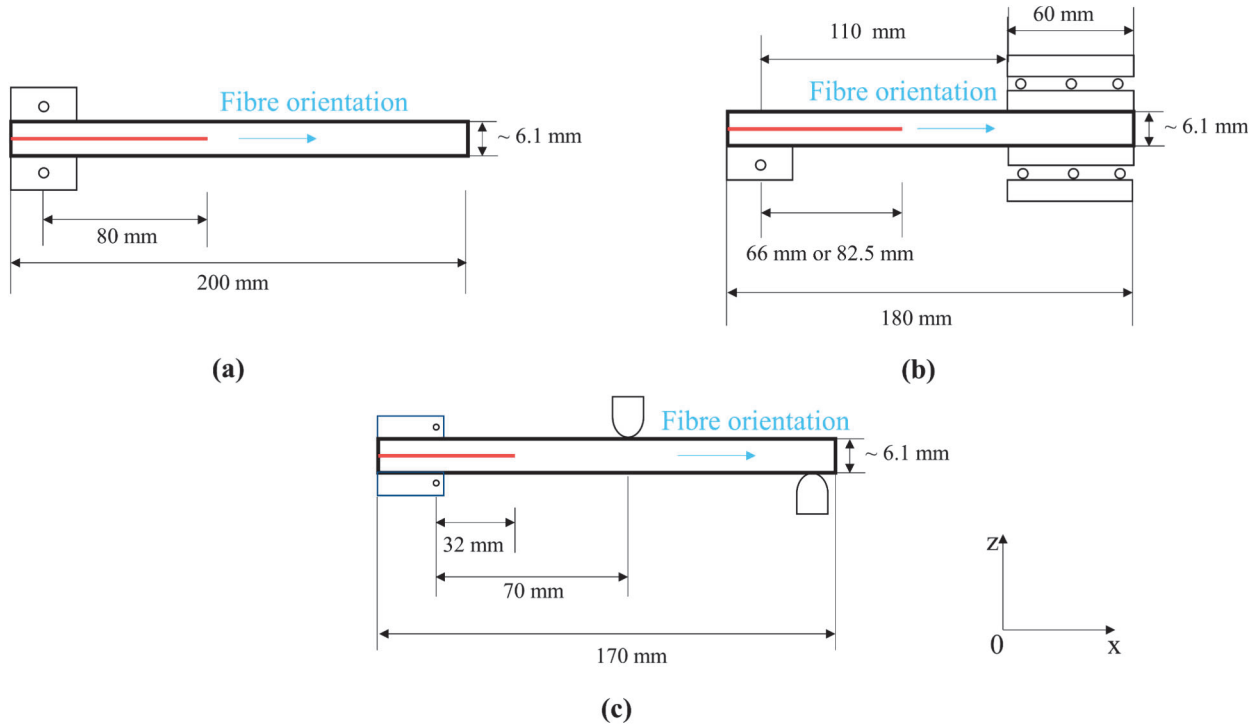

Fig. 2. Schematic of specimen design for mode I DCB tests (a), mode II ELS tests (b), and mixed-mode I/II MMB tests (c).

initial crack length for MMB specimens was set to 32 mm and L was set to 70 mm during the tests (Fig. 2 (c)). In the present work, crack length was measured from the load line to the crack front.

As shown in Fig. 2, depending on the test apparatus, aluminium blocks with dimensions of 20 mm (length) × 25 mm (width) × 15 mm (thickness) with a hole in the centre were used for applying load on DCB and ELS specimens, while the ones with dimensions of 20 mm (length) × 25 mm (width) × 6 mm (thickness) with a hole near the right end were used for load introduction on MMB specimens. A two-part epoxy adhesive, LOCTITE EA 3430, was applied to glue the loading blocks to the laminated pultruded composite plates. Before bonding, the surfaces of the aluminium blocks were treated by sand blasting, and all bonding surfaces of aluminium blocks and pultruded plates were cleaned using acetone. After bonding, specimens were later cured at room temperature for at least 24 h.

In the present work, DCB and ELS specimens were labelled using the following coding system: test apparatus (i.e. DCB or ELS) – manufactured panel (i.e. A or C) – specimen ID (e.g. #1). The MMB specimens were named as: test apparatus (i.e. MMB) – mixed-mode ratio (i.e. 0.33 or 0.67) – manufactured panel (i.e. B or C) – specimen ID (e.g. #1). The details of all samples for each test apparatus are listed in Table 2, containing the manufactured panel, the width, the initial crack length and the pre-cracking strategy.

2.2. Experimental set-ups and procedures

According to ASTM D5528 [6] for pure mode I interlaminar fracture, ISO 15114 [7] for pure mode II interlaminar fracture, and ASTM D6671 [9] for mixed-mode I/II interlaminar fracture, three types of beam specimens (Fig. 2) were tested under displacement control on a Zwick 10 kN universal testing machine combining DCB, ELS or MMB test apparatuses (Fig. 3), accordingly. DCB and ELS tests were performed under displacement control at 1 mm/min and MMB tests at 0.5 mm/min until complete delamination or maximum crack length limits recommended by the test standards were reached [6,7,9]. Three to seven specimens were repeated for each type of test. Before testing, white paint was applied to the side of each specimen for tracking the crack front, on top of which a crack length gauge with an increment of 1 mm was bonded. During testing, an OPTOMOTIVE camera with a resolution of 2048 × 2048 pixels was placed in the front of the testing machine to capture the history of crack length every 1–5 s. The corresponding load and displacement were recorded for each image. To reduce the effect of the resin pocket at the tip of the initial crack on fracture properties, pre-cracking can be beneficial. Three pre-cracking strategies were tried in this research, consisting of: (1) mode I loading using the DCB test rig at a displacement rate of 1 mm/min until the crack propagated 1–5 mm, (2) manually pre-cracking in mode I by inserting a plastic wedge into the interface, and (3) not applying any pre-cracking. After testing, the altitude map and roughness of both the top and bottom fracture surfaces were inspected by Keyence VR-5000 microscope.

The lever length of the MMB test apparatus c [9], i.e. the distance from the load line to the middle support contacting to the upper arm (Fig. 3(c)), was adjusted to 45 mm and 80 mm to create the mode mix ratio of ~ 0.33 and ~ 0.67, respectively. For the mixed-mode bending tests, the change of the distance c from the load line to the middle support contacting to the upper arm can cause different mixed-mode ratio G_{II}/G_T (G_{II}: mode-II strain energy release rate (SERR); G_T: total SERR). A large c leads to mode-II dominant fracture

Table 2
Details of all samples for each test apparatus involved in the present study (G_{II}/G_T: mixed-mode ratio; b: *specimen width*; a_0: initial crack length).

Specimen ID	G_{II}/G_T	Manufactured panel	b (mm)	a_0 (mm)	Pre-cracking strategy
DCB-A-#1	0.00	Panel A	25.07	91.0	Not applied as the resin pocket cracking at the tip can be identified as the first force drop through force–displacement curves
DCB-A-#2			24.93	96.0	Manually pre-cracking in mode I
DCB-A-#3			24.99	88.25	Not applied as the resin pocket cracking at the tip can be identified as the first force drop through force–displacement curves
ELS-A-#1	1.00	Panel A	20.02	83.5	Mode I loading using the DCB test rig
ELS-A-#2			19.99	86.5	Mode I loading using the DCB test rig
ELS-A-#3			19.87	68.3	Mode I loading using the DCB test rig
ELS-A-#4			20.03	69.2	Mode I loading using the DCB test rig
ELS-A-#5			17.47	72.6	Manually pre-cracking in mode I
ELS-C-#5		Panel C	20.36	71.2	Mode I loading using the DCB test rig
ELS-C-#7			19.63	68.0	Mode I loading using the DCB test rig
MMB-0.33-C-#1	0.33	Panel C	24.11	36.8	Mode I loading using the DCB test rig
MMB-0.33-C-#2			26.09	35.0	Mode I loading using the DCB test rig
MMB-0.33-C-#3			25.76	35.5	Mode I loading using the DCB test rig
MMB-0.33-B-#4		Panel B	24.68	34.7	Mode I loading using the DCB test rig
MMB-0.33-B-#5			25.55	36.5	Mode I loading using the DCB test rig
MMB-0.33-B-#6			25.52	37.5	Mode I loading using the DCB test rig
MMB-0.67-C-#1	0.67	Panel C	25.41	35.8	Mode I loading using the DCB test rig
MMB-0.67-C-#2			24.54	34.7	Mode I loading using the DCB test rig
MMB-0.67-C-#3			25.58	35.8	Mode I loading using the DCB test rig
MMB-0.67-B-#4		Panel B	25.13	32.0	Not applied due to detachment of a loading block during the DCB tests
MMB-0.67-B-#5			25.55	39.0	Mode I loading using the DCB test rig

and a small c creates mode-I dominant fracture. Based on the ASTM D6671 test standard [9], the relation between c and G_{II}/G_T considers the correction for lever weight that can affect the mode mixture in the present study, as shown below:

$$c = \left(1 + \frac{P_g}{P_{est}}\right) \frac{12\beta^2 + 3\alpha + 8\beta\sqrt{3\alpha}}{36\beta^2 - 3\alpha} L - \frac{P_g}{P_{est}} c_g \tag{1}$$

where

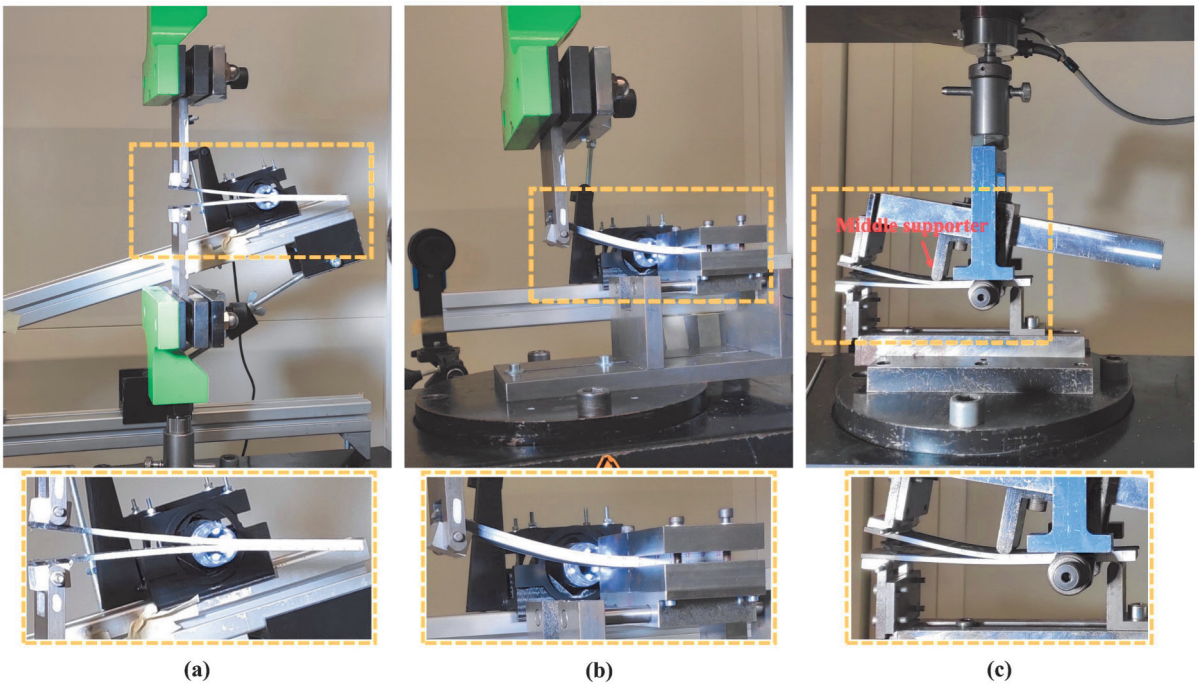

Fig. 3. Double cantilever beam (a), end-loaded split (b) and mixed-mode bending (c) test apparatuses.

$$\alpha = \frac{1 - \frac{G_{II}}{G_T}}{\frac{G_{II}}{G_T}} \tag{2}$$

$$\beta = \frac{a + \chi h}{a + 0.42\chi h} \tag{3}$$

$$\chi = \sqrt{\frac{E_{11t}}{11G_{13}}\left\{3 - 2\left(\frac{\Gamma}{1+\Gamma}\right)^2\right\}} \tag{4}$$

$$\Gamma = 1.18\frac{\sqrt{E_{11t}E_{22t}}}{G_{13}} \tag{5}$$

In Eq.1, P_{est} is the estimated value of critical load which was 500 N and 1200 N for the mixed mode ratio of 0.33 and 0.67 respectively, according to the preliminary tests; P_g is the weight of lever and attached apparatus (13.32 N for the present study); c_g is the lever length to the centre of gravity (45 mm for the present study); L is the half-span length of the MMB test apparatus (70 mm for the present study). Besides, α in Eq.2 is related to the mixed-mode ratio G_{II}/G_T. In Eq. (3), a is the delamination length, and h is half of thickness. In Eq.4 and Eq.5, E_{11t}, E_{22t} and G_{13} are material properties listed in Table 1. Thus, for a given G_{II}/G_T, α can be obtained which can be later used to calculate the c.

Overall, four mode mix ratios, i.e. 0.00 (pure mode I), ~0.33, ~0.67 and 1.00 (pure mode II), were achieved in the present work. The mixed-mode ratio here denotes the ratio of mode II strain energy release rate (SERR) G_{II} to the total SERR G_T.

2.3. Calculation of strain energy release rates

For the pure mode I strain energy release rate G_I, Table 3 lists three data reduction methods as mentioned in the ASTM D5528 test standard [6], i.e. Modified Beam Theory (MBT), Compliance Calibration (CC), and Modified Compliance Calibration (MCC) for DCB tests. All these standardised methods were used and compared in the present study. In Table 3, P is the applied load and δ is the load point displacement, which were recorded by the testing machine. C is the compliance and can be calculated as δ/P. a is the crack length at the interface between the loading line and the crack tip that was monitored by the camera. b is the specimen width and h is the half specimen thickness. Related fitting parameters Δ, n, A^1 can be experimentally determined as detailed in Table 3, and their values are listed in Table A1.

As for the pure mode II strain energy release rate G_{II}, three data reduction methods, i.e. Experimental Compliance Method (ECM), Simple Beam Theory (SBT) and Corrected Beam Theory using Effective crack length (CBTE), as mentioned in the ISO 15114 test standard for ELS tests [7], were employed and compared in the present study. Table 4 lists the formula for each method. Here, P, δ, C, a, b, h have the same meanings as above-mentioned for DCB tests. a_e is the effective crack length calculated based on the corrected beam theory, rather than experimental observations. For the SBT and the CBTE methods, E_1 is the flexural modulus that was obtained by experimentally performing the clamp calibration procedure described in the test standard [7], where the free length L_{free} of 50 mm, 60 mm, 70 mm, 80 mm, 90 mm, 100 mm and 110 mm was set sequentially. In the present study, the slope and intercept of the linear regression to the $C^{1/3}$ versus free length L_{free}, based on the clamp calibration procedure, are 0.0017 and 0.0451 respectively. As a result, Δ_{clamp} for the CBTE method, as mentioned in Table 4, is 26.53 mm. Table A2 lists the values of m and E_1 for each ELS specimen.

Regarding MMB tests, the method proposed in ASTM D6671 [9] was followed to calculate the mode I component G_I (See Eq. (6) and the mode II component G_{II} (See Eq. (7) of the energy release rate G_T for mixed-mode ratios of 0.33 and 0.67, where G_T=G_I+G_{II}. Here, P, a, b, and h have the same meanings as above-mentioned for DCB tests. L is the half-span length of the MMB test apparatus and it is 70 mm as mentioned in Section 2.1. c is the distance from the load line to the middle support contacting to the upper arm (Fig. 3(c)), which is set to 45 mm and 80 mm for the mode mix ratio of ~ 0.33 and ~ 0.67, respectively (Section 2.2). χ is the crack length correction parameter (see Eq. (4). E_{1f} is the bending modulus of the MMB specimen (see Eq.8). In Eq. (8), c_{sys} is the system compliance that was measured following the procedure in the standard [9] by using a rectangular steel bar in the MMB apparatus. It is 6.37E-4 mm/N and 3.16E-4 mm/N under the mode mix ratio of 0.33 and 0.67, respectively. Besides, m_1 is the slope of load-displacement curve and a_0 is the initial crack length (i.e. 32 mm). Table A3 lists the values of E_{1f} for each MMB specimen.

Table 3
Three data reduction methods to calculate mode I strain energy release rates based on the ASTM D5528 test standard [6].

Data reduction methods	Equations	Notes
Modified Beam Theory (MBT)	$G_I = \frac{3P\delta}{2b(a+\lvert\Delta\rvert)}$	Δ is the intercept of the least square plot of $C^{1/3}$ as a function of a.
Compliance Calibration (CC)	$G_I = \frac{nP\delta}{2ba}$	n is the slope of the least square plot of $\log(C)$ as a function of $\log(a)$.
Modified Compliance Calibration (MCC)	$G_I = \frac{3P^2C^{2/3}}{4A^1bh}$	A_1 is the slope of the least square plot of $a/2h$ as a function of $C^{1/3}$.

Table 4
Three data reduction methods to calculate mode I strain energy release rates based on the ISO 15114 test standard [7].

Data reduction methods	Equations	Notes
Experimental Compliance Method (ECM)	$G_{II} = \frac{3P^2a^2m}{2b}$	m is the slope of the least square plot of C as a function of a^3.
Simple Beam Theory (SBT)	$G_{II} = \frac{9P^2a^2}{4b^2h^3E_1}$ $E_1 = \frac{1}{2b(h \times slop)^3}$	E_1 can be deduced from the slope (i.e. 0.0017 $1/(N^{1/3} \times mm^{2/3})$) of the linear regression to the $C^{1/3}$ versus free length L_{free}, obtained by experimentally performing the clamp calibration procedure described in [7].
Corrected Beam Theory using Effective crack length (CBTE)	$G_{II} = \frac{9P^2a_e^2}{4b^2h^3E_1}$ $a_e = \left[\frac{1}{3}\left\{2bCh^3E_1 - \left(L + \Delta_{clamp}\right)^3\right\}\right]^{\frac{1}{3}}$ $E_1 = \frac{1}{2b(h \times slop)^3}$	E_1 is the same as in SBT. Δ_{clamp} is the ratio of the intercept to the slope (i.e. 26.53 mm) for the linear regression to the $C^{1/3}$ versus free length L_{free}, obtained by experimentally performing the clamp calibration procedure described in [7].

$$G_I = \frac{12P^2(3c-L)^2}{16b^2h^3L^2E_{1f}}(a+\chi h)^2 \tag{6}$$

$$G_{II} = \frac{9P^2(c+L)^2}{16b^2h^3L^2E_{1f}}(a+0.42\chi h)^2 \tag{7}$$

$$E_{1f} = \frac{8(a_0+\chi h)^3(3c-L)^2 + \left[6(a_0+0.42\chi h)^3 + 4L^3\right](c+L)^2}{16L^2bh^3\left(\frac{1}{m_1} - c_{sys}\right)} \tag{8}$$

3. Results

This section presents force–displacement response and crack length-displacement response under modes I, II, and mixed-mode I/II. Besides, the delamination resistance curves are reported for each loading mode. Based on microscopic inspection of fracture surfaces, failure modes are also described for a deep understanding of the fracture behaviours of laminated pultruded plates.

3.1. Mode I DCB tests

Fig. 4(a) shows the force–displacement curves for the three DCB specimens. Of these specimens DCB-A-#1 and the DCB-A-#3 were not pre-cracked and DCB-A-#2 was manually pre-cracked, achieving a pre-crack length a-a_0 = 10 mm. Thus, a sudden force drop occurred for DCB-A-#1 and DCB-A-#3 before reaching the maximum force value due to a resin pocket ahead of the initial crack insert.

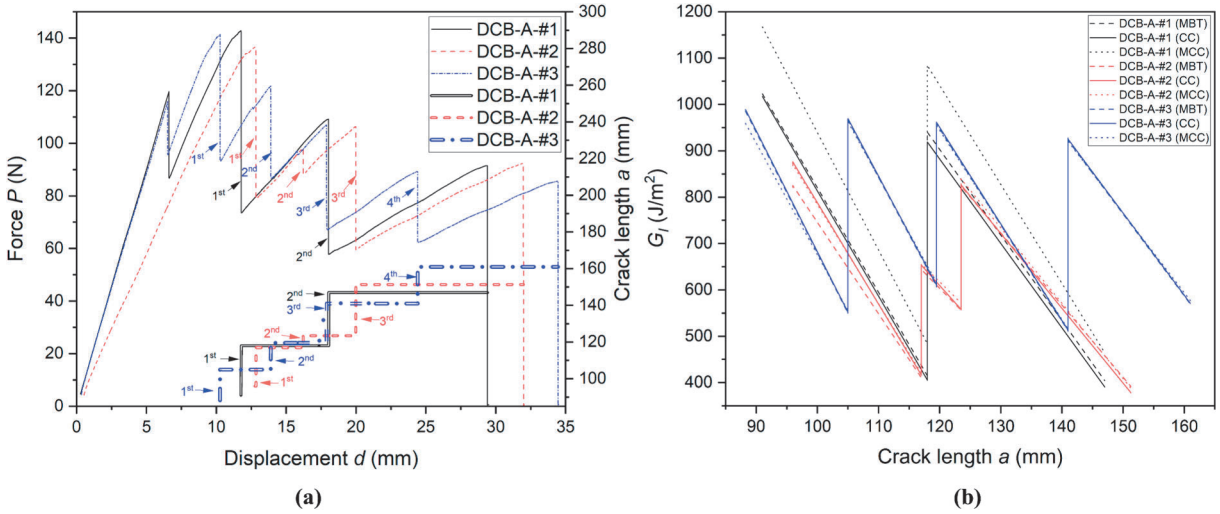

Fig. 4. History of force and crack length with the increase of displacement for DCB specimens (a); R-curves obtained from different methods recommended in ASTM D5528 [6] (b).

Overall, non-linearity of force–displacement curves appeared close to the maximum force where the crack initiated and propagated suddenly 10 mm to 30 mm, accompanying the abrupt reduction of force. After the first crack propagation, the force increased until the second crack propagation occurred when a sudden force drop was presented again. In other words, the accumulation of energy occurs to overcome the resistance generated near the crack tip and once this energy threshold is reached, both crack propagation and strain energy release occur [25]. Altogether, such rapid crack propagation occurred in two to four steps until the complete delamination of the specimen, i.e. the crack propagation can be characterised as brittle stick–slip type. Floros et al. [26] and Guo et al. [27] observed a similar phenomenon for composite adhesive joints, which is attributed to that fact that the fracture toughness in crack initiation stage is greater than that in crack propagation stage. As a result, the crack propagation instead of being continuous, behaves as a succession of rapid propagation and arrest phases [28]. R-curves (i.e. crack length versus SERR) in Fig. 4(b) showed that SERR seems to decrease slightly with the increasing crack length, while a plateau is not evident. Additionally, it can be seen that the three different data reduction (see Table 3) methods give very similar values of SERR. The only exception is that a slightly high value of SERR can be observed for DCB-A-#1 using the Modified Compliance Calibration method. As only two crack propagations can be taken into account before full delamination for DCB-A-#1, fewer data points are available for reliable parameter fittings listed in Table 3 to accurately calculate the SERR. This may explain the discrepancy.

Fig. 5 shows the fracture morphology and altitude map of the bottom fracture surfaces of each specimen. In the altitude map, the blue indicates low positions, and the red represents high positions. Caused by the energy accumulation and friction at the crack tip before subsequent propagation, the delamination fronts were marked by dark dashed lines in Fig. 5. Here, the white dashed line was used to indicate the delamination front formed by opening the resin pocket ahead of the initial crack insert, which was generated by either pre-cracking before DCB testing or the direct DCB testing without pre-cracking. To remove the effect of resin pocket on fracture behaviours, the crack propagation, the front of which was marked by the white dashed lines, was discarded during the analysis. As for the failure mode of such bonded plates, cohesive failure, adhesive failure, and substrate failure [29] proposed for the fracture surface analysis of adhesive joints can be exploited to uncover their interlaminar fracture behaviours further [30]. Fig. 5 demonstrates that cohesive failure within the bond layer is the dominant failure mode. Some local spots showing dark blue in the altitude map suggest adhesive failure at the interface between the pultruded plate surface and the bonded layer. The substrate failure can be observed at the locations indicated by the white arrows in Fig. 5, showing evidence of peeling off of CFRP strips from the pultruded plate. The occurrence of substrate failure suggests that the mechanical strength of the substrate (i.e. pultruded plate) at local regions is lower than the interfacial bond strength [29]. The increment of crack length during each propagation is similar, except for a smaller crack-length increase during the second propagation for DCB-A-#2 due to the relatively irregular crack front generated from manual pre-cracking and DCB-A-#3 caused by the early substrate failure.

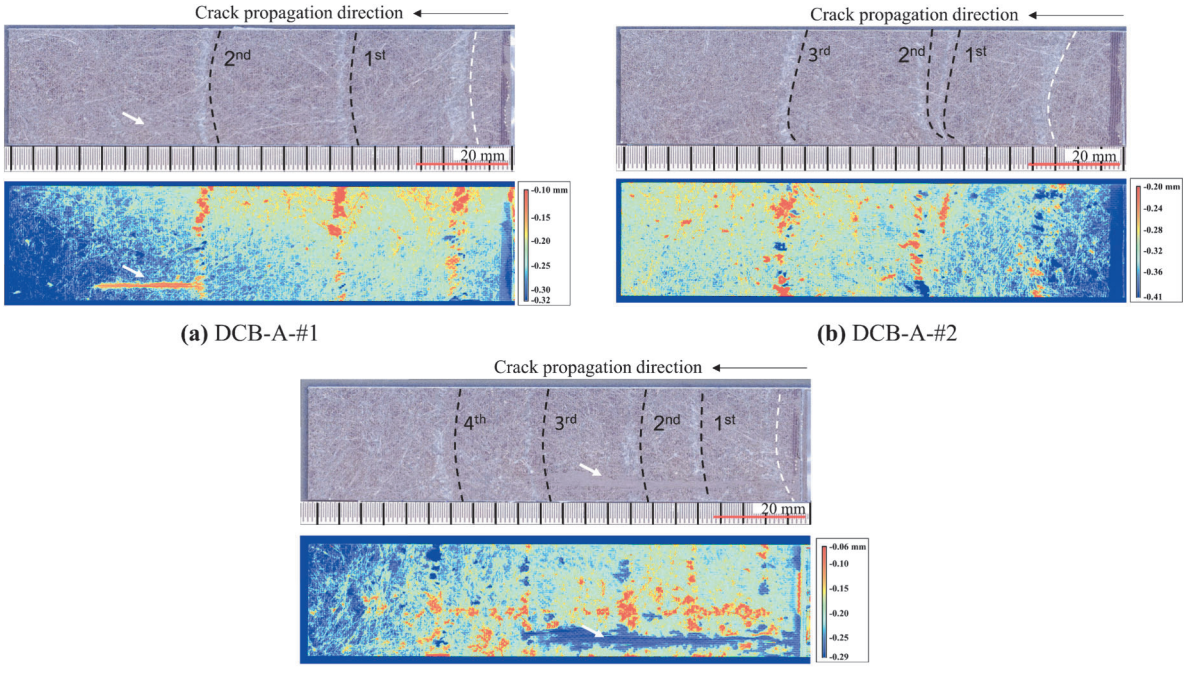

Fig. 5. Failure morphology and altitude map of bottom fracture surface obtained from microscopic inspection for the specimen DCB-A-#1 (a), DCB-A-#2 (b), and DCB-A-#3 (c). (Note: the distance between two black solid lines on the reference rule is 5 mm.).

3.2. Mode II ELS tests

Fig. 6(a)) shows the force–displacement curves for the seven ELS specimens. In contrast to mode I DCB tests, a non-linearity can be observed from a smaller displacement threshold, along with more stable crack propagation. During the post-peak stage, most of the ELS specimens presented a gradual decrease in force. At the same time, the mode-II crack continued propagating until its tip was close to the clamp of the ELS test fixture. After a while, the force increased showing that the clamping started to affect crack propagation, and the test should be terminated soon [31]. An exception exists regarding the post-peak trend of force–displacement curves, i.e. ELS-A-#1 and ELS-A-#2, which have a longer initial crack length, 82.5 mm, compared with 66 mm for others. The continuous force increase for these two specimens is attributed to inadequate space for crack propagation, which is significantly affected by the ELS fixture. Therefore, they were excluded in the following analysis. Besides, a lower maximum force and slower increase of force during the pre-peak stage was presented in Fig. 6(a) for ELS-A-#5 [32]. This phenomenon is attributed to the fact that its width (i.e. 17.47 mm), is smaller than those of other ELS specimens ranging from 19.63 mm to 20.36 mm (Table 2).

To eliminate the effect of clamping on the mode-II fracture properties, the crack length was measured from the initiation to the moment when the valley of force–displacement curves at the post-peak stage was reached. Fig. 6(b)-(d) shows the mode-II delamination resistance obtained from three data reduction methods (see Table 4) recommended in ISO 15114 [7] with increasing crack length. An abrupt rise of SERR can be noticed during the early crack propagation with an increment of crack length of less than 2 mm, after which a gradual growth of SERR is exhibited without reaching a plateau for most specimens. A noticeable saturation of the SERR only occurred for specimen ELS-A-#4 when using the CBTE method [7]. The above-mentioned differences of ELS-A-#5, in both the pre-cracking and the width, have little effect on the calculation of mode-II SERR (Fig. 6(b)-(d)). Among these different methods to calculate mode-II SERR, SBT and CBTE depends on an analytical calculation of the compliance while ECM is based on the quality of the fitting of the measured compliance [15]. As SBT did not involve the correction for beam root deflections, rotations at either the crack tip or clamping point, and the transverse shear effects in the composite arms, a lower SERR is presented compared with the similar results obtained from ECM and CBTE. Except for the CBTE methods, the history of crack length determined from experiments is a must for both ECM and SBT methods. However, accurate localisation of mode-II crack tip is a remaining challenge [33,34], promoting the use of the CBTE method for this type of pultruded plates. The only complexity of the CBTE method may be experimentally calibrating the ELS

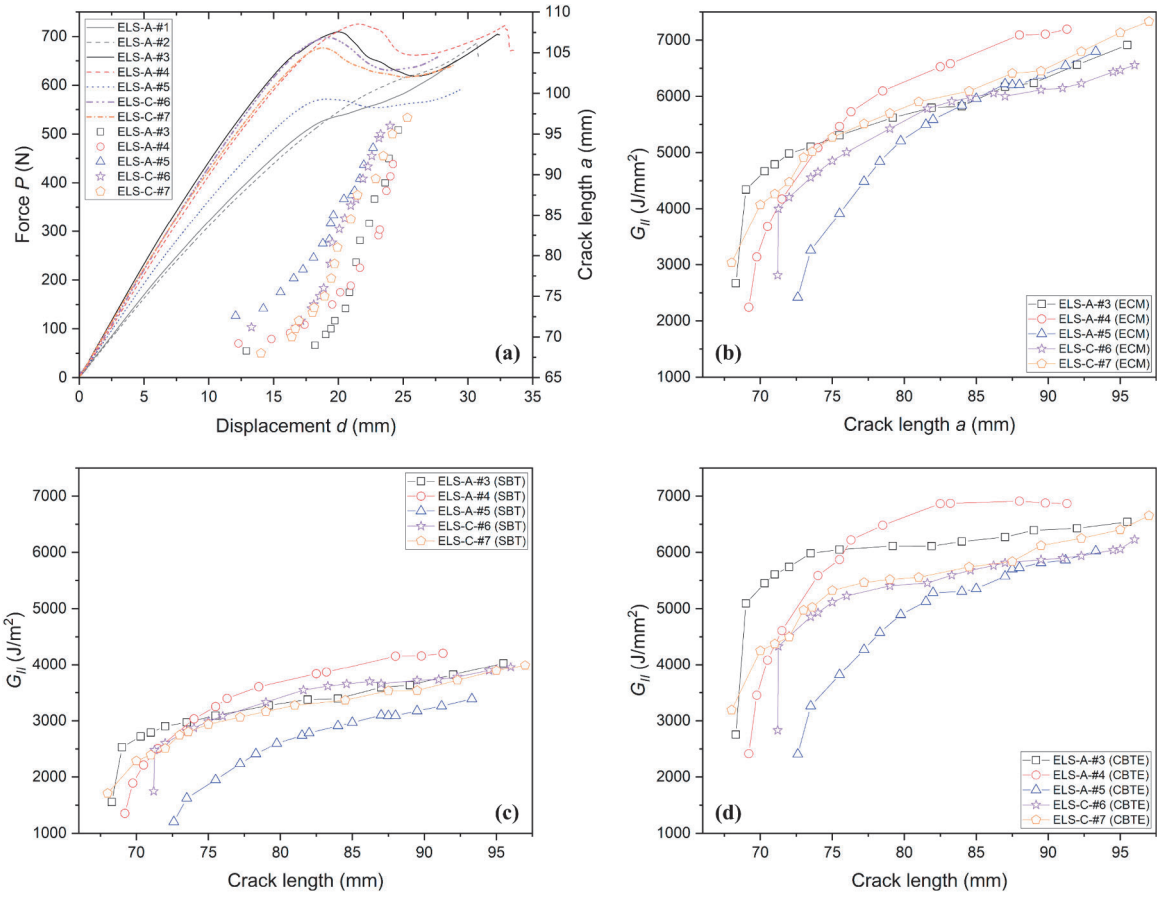

Fig. 6. History of force and crack length with the increase of displacement for ELS specimens (a); R-curves obtained from the ECM method [7] (b); R-curves obtained from the SBT method [7] (c); R-curves obtained from the CBTE method [7] (d).

fixture by setting different types of free lengths of the ELS specimen [7] to obtain the corresponding parameters, e.g. flexural modulus.

Fig. 7 shows the failure morphology and altitude map of the bottom fracture surface, where cohesive failure within the bond layer is the main failure mode. The prevalence of cohesive failure can be attributed to the formation (Stage I), growth (Stage II) and subsequent coalescence (Stage III) of cusps during mode II shear loading, as shown in Fig. 8. This process involves the development of an elongated process zone characterised by multiple shear planes at 45°, making the joint more susceptible to cohesive failure than adhesive or substrate failure [35]. Consequently, tortuous fracture surfaces were generated by mode II cohesive failure. As also suggested in [36], the cusp formation and deformation during mode II fracture contributes to dominant energy absorption, which is considered as the main reason why mode II fracture toughness greatly exceeds mode I fracture toughness in thermosetting carbon-fibre reinforced composites.

3.3. Mixed-mode I/II MMB tests

Different from DCB and ELS specimens, which were defect-free (Panel A and Panel C), MMB specimens were cut from Panel B and Panel C, where Panel B contained manufacturing-induced defects (Fig. 1(b)). Crack measurements for MMB tests were halted when either (i) the crack propagated to the middle support in a stable manner (see Fig. 2(c)), or (ii) unstable crack growth occurred, accompanied by a sudden drop of force.

For the mode mix ratio G_{II}/G_T=0.33, the force–displacement curves started to become non-linear after the crack was initiated, and a sudden drop of force was exhibited for most specimens after reaching the maximum force (Fig. 9 (a)). As they are defect-free, MMB-0.33-C-#2 and MMB-0.33-C-#3 showed relatively stable propagation in comparison with specimens with defects. Consequently, too few data points were obtained to plot R-curves for most MMB specimens (Fig. 10(a)). The final failure of all specimens with the ratio of G_{II}/G_T=0.33 exhibited unstable crack propagation through the mid-support of the MMB test apparatus along with an abrupt drop of force.

Regarding the G_{II}/G_T=0.67 tests, the non-linearity of force–displacement response before reaching the peak force is more evident than G_{II}/G_T=0.33 (Fig. 9 (b)). Besides, all specimens gradually decreased force at the post-peak stage. Meanwhile, as it is dominated by mode II fracture behaviours, the crack propagation behaves more stable than that when employing the lower mixed-mode ratio. Fig. 10 (b) shows the increase of delamination resistance along with crack propagation. A plateau of SERR seems to be reached soon by MMB-0.67-B-#4 and MMB-0.67-B-#5, whereas the SERR of other specimens barely turns to saturation along with crack propagation. Apparently, defect-free specimens need longer crack propagation so that the R curve can reach the saturation in comparison with those with defects. For MMB-0.67-B-#4, force and SERR are slightly higher than those from other specimens (Fig. 9 (b) and Fig. 10(b)). This is because pre-cracking over 2 to 5 mm was generated by performing DCB tests for all MMB specimens, except MMB-0.67-B-#4 which was not pre-cracked due to the detachment of a loading block during the DCB tests.

Fig. 11 and Fig. 12 present the results of microscopic inspection at either the top or the bottom fracture surfaces for the mixed-mode specimens. Cohesive failure is dominant at the crack propagation region in the length of 5–14 mm for G_{II}/G_T=0.33, while adhesive failure and substrate failure exist at some local regions. Adhesive failure can be recognised by blue spots in the altitude map, as shown

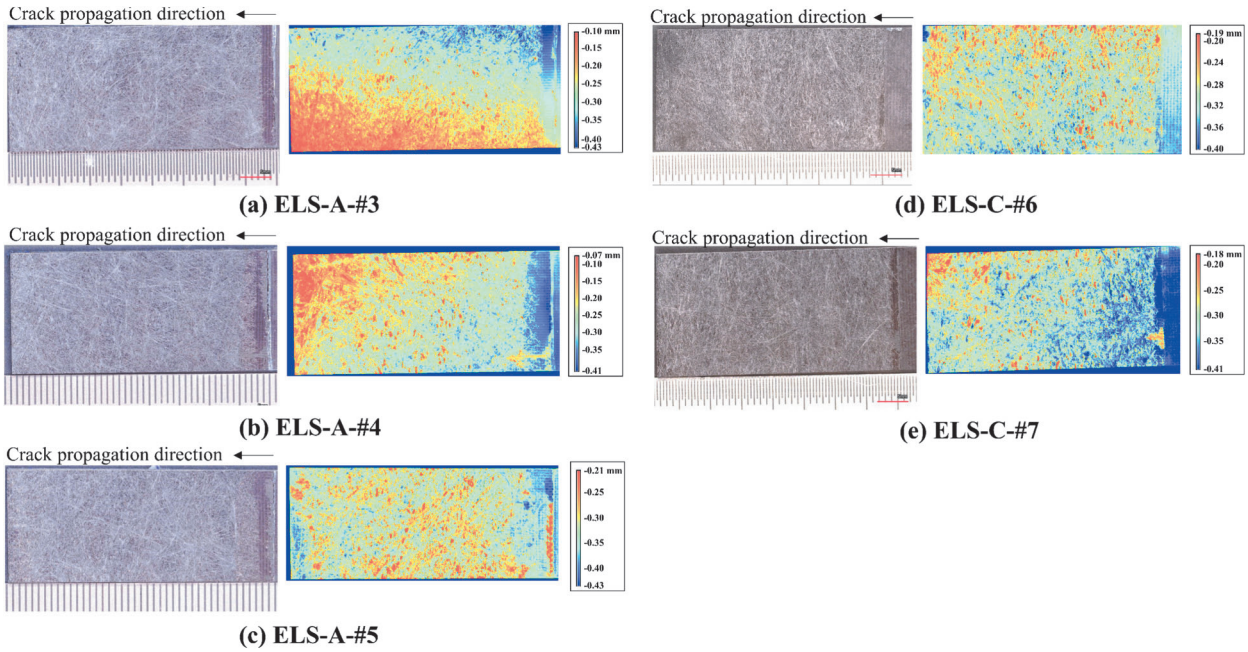

Fig. 7. Failure morphology and altitude map of bottom fracture surface obtained from microscopic inspection for ELS specimens.

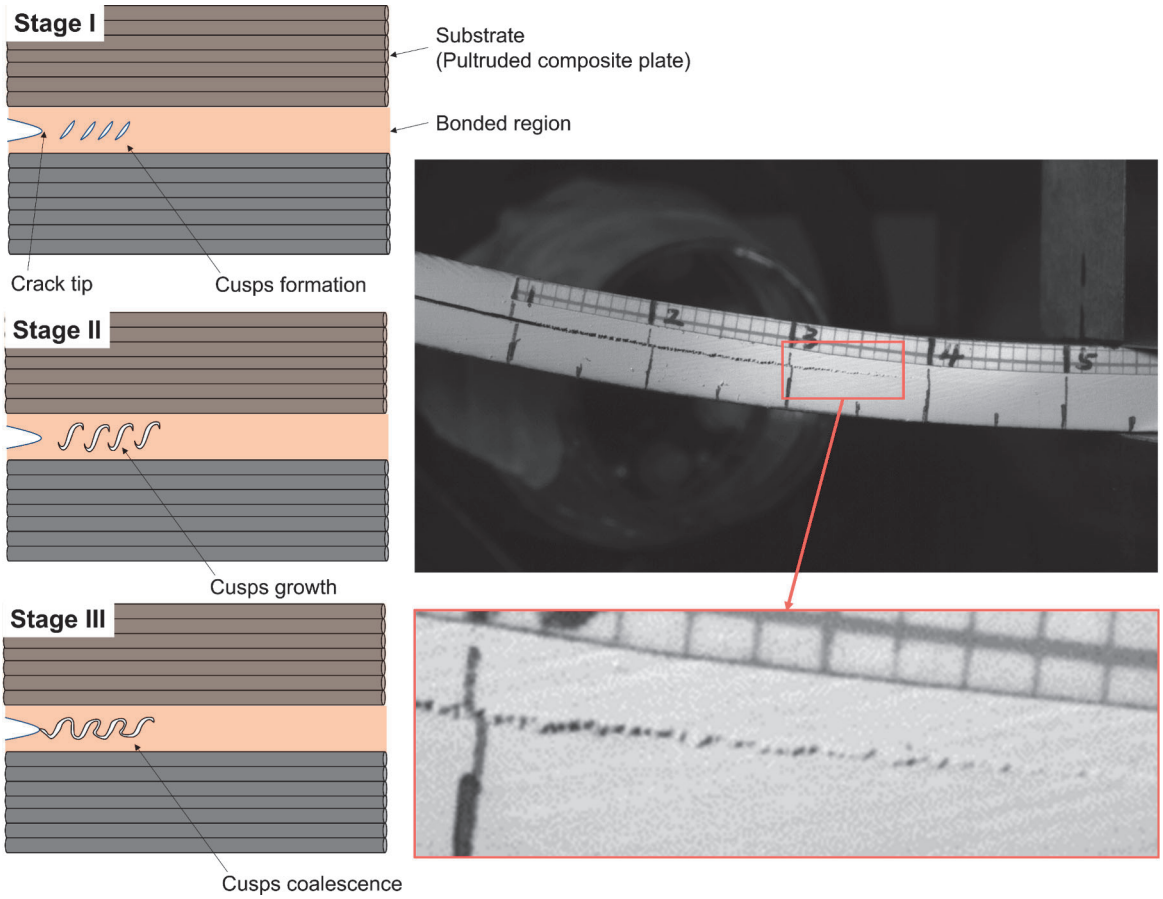

Fig. 8. Cusps' formation, growth and coalescence under mode II fracture.

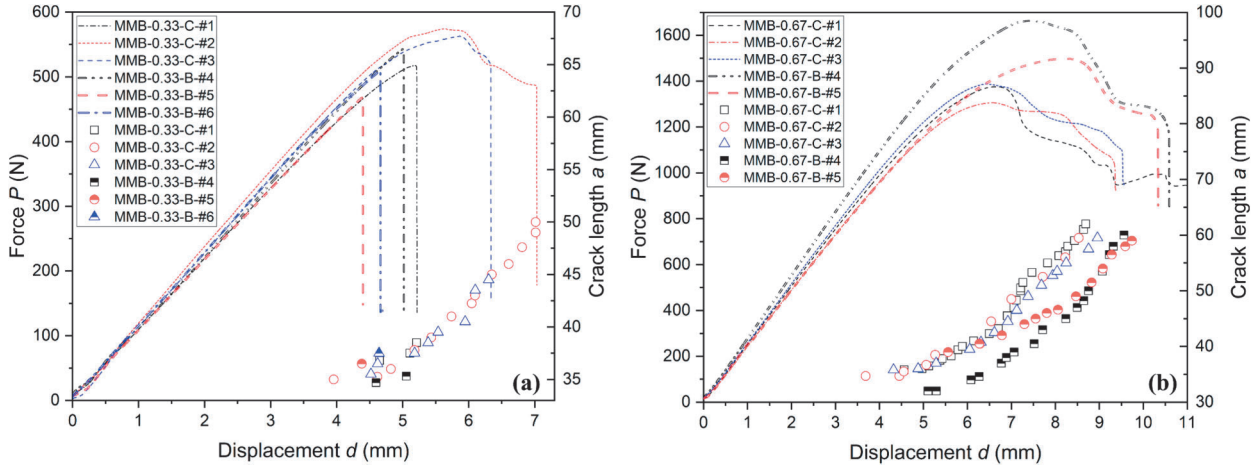

Fig. 9. History of force and crack length with displacement increase for MMB specimens tested at the mixed mode ratio 0.33 (a) and 0.67 (b).

within the white circled region in Fig. 11. The white arrows in Fig. 11(d) and (f) mark substrate failure. After the onset of cohesive failure, crack growth instability (abrupt crack propagation) occurs in the adhesive region, indicating mode I dominance. As for G_{II}/G_T=0.67, cohesive failure is the main failure mode due to the higher contribution of shear failure in mode II. For both mode mix ratios, the interlaminar crack jumped to the interface between the bond layer and the pultruded plate when the final failure occurred, forming a large area with adhesive failure. Dashed lines in Fig. 11 and Fig. 12 are used to indicate the crack front before the final failure, which

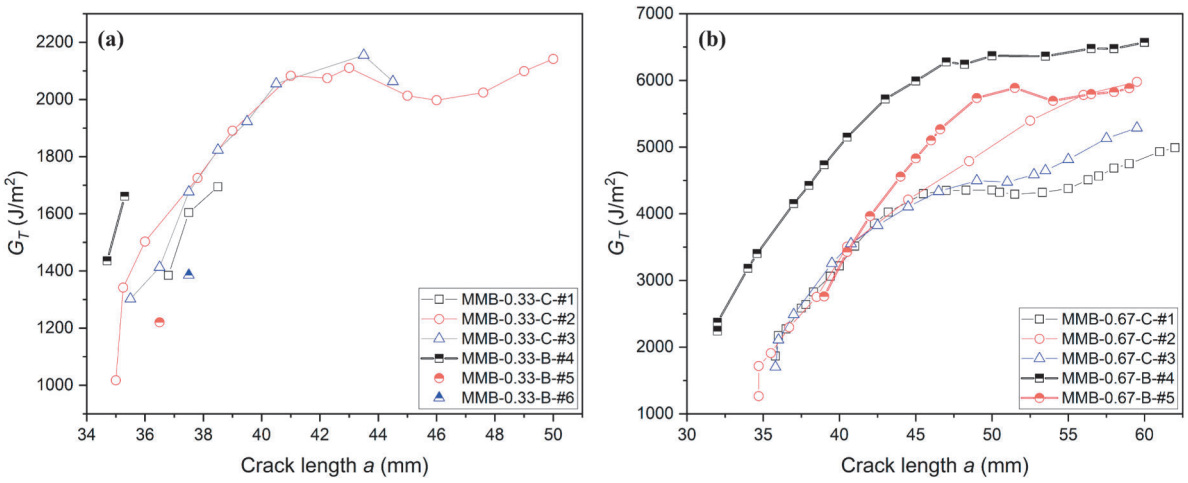

Fig. 10. R-curves of MMB specimens tested at the mixed-mode ratios 0.33 (a) and 0.67 (b).

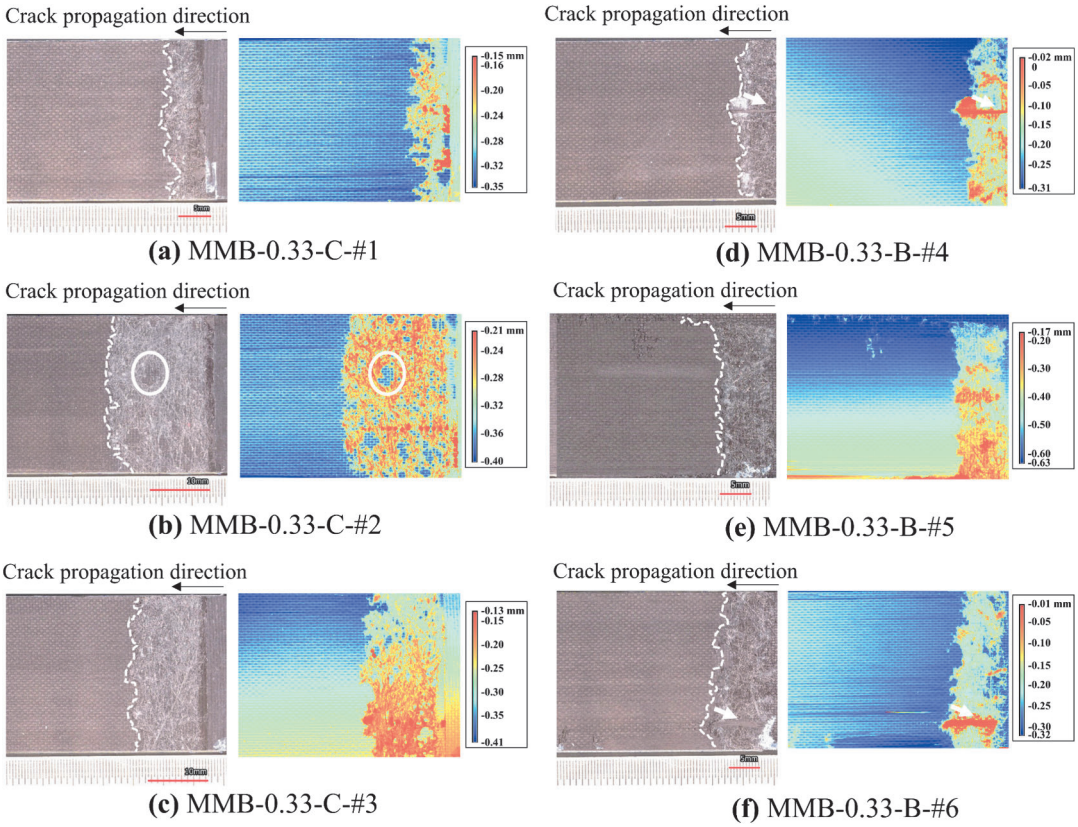

Fig. 11. Failure morphology and altitude map of top fracture surface obtained from microscopic inspection for MMB specimens tested at the mixed-mode ratio 0.33.

is less straight for specimens from Panel B due to the manufacturing-induced defects. Overall, depending on whether mode I or mode II is more dominant, the force–displacement response, the stability of crack propagation, and the fractography of MMB specimens under the mixed-mode I/II loading condition are prone to be more similar to pure mode I or pure mode II.

4. Discussion

Based on the fracture properties characterised by DCB, ELS and MMB tests, the mixed-mode I/II failure criteria can be established

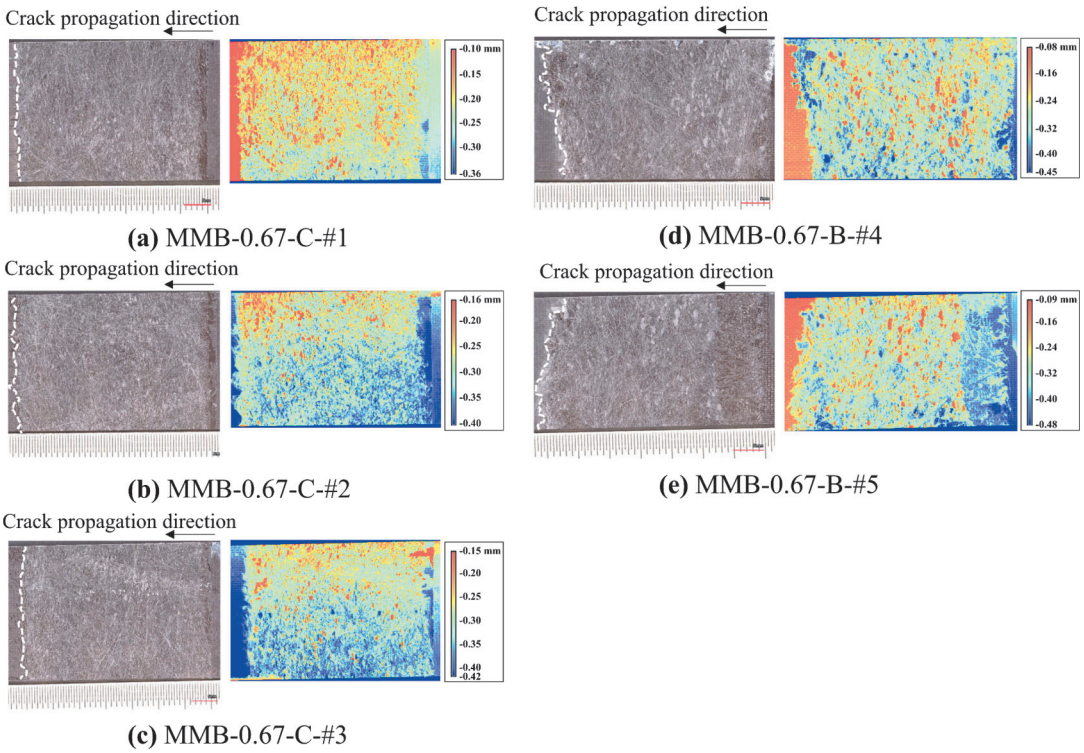

Fig. 12. Failure morphology and altitude map of bottom fracture surface obtained from microscopic inspection for MMB specimens tested at the mixed-mode ratio 0.67.

for pultruded composite plates. Besides, the applicability of testing standards [6,7,9] followed in the present study is discussed. Also, the mixed-mode I/II fracture behaviour of MMB specimens with and without manufacturing-induced defects is compared in this section.

4.1. Mixed-mode I/II failure criteria

From the performed experiments failure criteria for crack initiation toughness at any mode-mix could be determined using either the Benzeggagh-Kenane (B-K) or power law criteria [16,37,38]. Propagation fracture toughness could not be determined as almost all R-curves obtained from the DCB, ELS and MMB tests did not present a clear plateau.

According to the standards [6,7,9], three methods can define the interlaminar crack initiation: (1) the point of deviation from linearity in the force–displacement curve (NL); (2) the point where the compliance has increased by 5 % or the force has reached a maximum value (5 %/max); or (3) the point at which delamination is visually observed (VIS). Based on these criteria, the corresponding SERR was calculated using different data reduction methods. For pure mode I, the critical SERR obtained from the compliance calibration method was used to generate the failure criteria, as the fitting parameter n is similar among DCB specimens compared with those (i.e. Δ and A^1) from other methods (Table A1). As for pure mode II, the critical SERR calculated by the CBTE method was employed in formulating the failure criteria as it gave a similar estimation as the ECM method and did not require any experimental crack length measurements.

Among the three methods to identify crack initiation, NL provides the most conservative measurement of critical SERR [39], significantly lower than that at 5 %/max and VIS which show similar critical SERR except under pure mode II (Table A4-Table A7). In Table A5, critical SERR under pure mode-II obtained at 5 % increase of compliance is lower than that at VIS for some of the specimens, which could be attributed to the clamping system of the ELS apparatus that adds extra flexibilities on the specimen before crack initiation. As a result, crack initiation for all types of fracture tests was identified at VIS.

The B-K (Fig. 13(a)) and power law criteria (Fig. 13(b)) can be used to describe the failure envelope under mixed-mode I/II, where the average G_{IC} is 960 J/m^2 and the average G_{IIC} is 2720 J/m^2 according to Table A4 and Table A5. In Fig. 13, only the MMB specimens without defects are involved in the curve fitting. All fits, whether using the B-K or power law criteria, present a high R-square value, demonstrating the capability of both criteria to describe the mixed-mode failure envelope at interfaces of such plates. Among three different fits by applying the power law criterion, the one with fitting parameters equal to 1.0 (Fitted 3 in Fig. 13(b)) indicates the possibility of a linear relation between the mixed-mode I/II fracture toughness components. Although this linear behaviour does not hold for the majority of cases of interlaminar fracture of CFRP composites, in the present case it may be a result of the secondary bonded nature of laminated pultruded plates, as suggested by Simon and Banks-Sills [37].

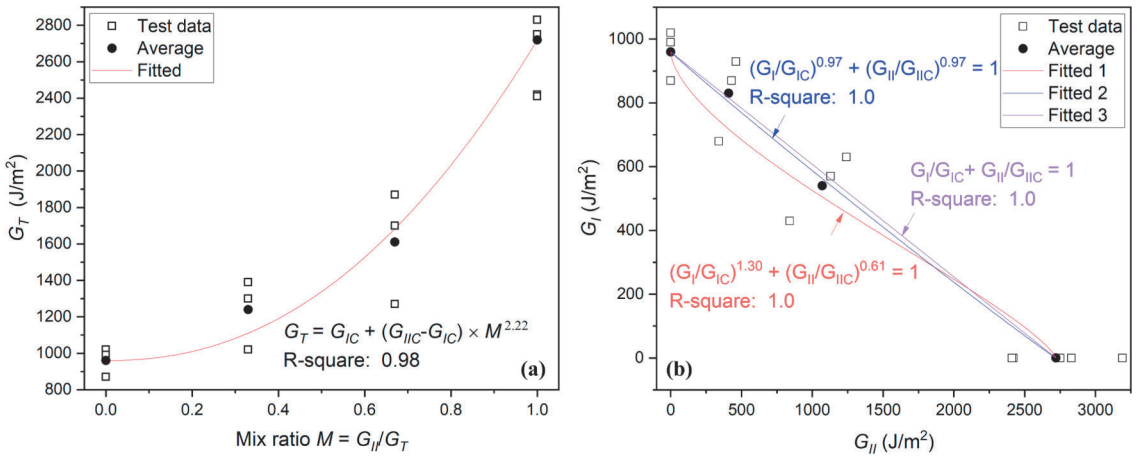

Fig. 13. Mixed-mode I/II failure criteria to evaluate the critical SERR at a specific mixed-mode ratio: (a) B-K criterion; (b) power law criterion.

4.2. Applicability of testing standards

Regarding the applicability of existing testing standards, the following relevant experiences can be reported based on the present work. For DCB tests, it is recommended to set a larger specimen length than that used in the present work so that more steps of crack propagation could exhibit in such laminated pultruded plates. Regarding ELS tests, attention should be paid to the clamping effect on crack propagation, which can be alleviated by introducing a short initial crack for a fixed free length. However, smaller initial crack length could lead to unstable crack propagation under mode II, as observed by Yan et al. [14]. Therefore, it is necessary to perform parametric studies about initial crack lengths for mode II fracture tests, especially in the cases that specimen dimensions are out of range recommended in the test standards. Besides, simple beam theory is not suggested for mode II fracture analysis as it predicts lower SERR compared with the other two data reduction methods available in ISO 15114 [7] (Fig. 6).

For mixed-mode I/II tests, detachment between loading blocks and MMB specimens could occur, even if standard bonding procedures were strictly followed [9]. This is due to the large force applied on the loading blocks to perform mixed-mode I/II fracture of such bonded composite plates. To alleviate this issue, the half-span length of the MMB test apparatus was set to 70 mm in the present work, while the test standard [9] recommends that it shall be 50 mm for composite laminates.

Overall, it seems that the pure mode I, pure mode II and mixed-mode I/II interlaminar fracture behaviour of laminated pultruded composite plates can be obtained accurately by following specimen design and test configurations introduced in ASTM D5528 [6], ISO 15114 [7] and ASTM D6671 [9]. However, it is found that there is a lack of criteria for determining crack initiation by visual observation in these testing standards, which could induce noticeable uncertainties for the SERR calculation. A tilted crack plane usually forms ahead of the pre-crack tip before mode-II or mixed-mode I/II crack propagation for the bonded composite plates (Fig. 14), which was orientated at 29°-35° based on the horizonal line for most of MMB specimens under mixed-mode I/II loading and orientated at 44°-50° based on the horizonal line for ELS specimens under pure mode II loading. The standards are not clear whether this should already be considered as visual crack growth. Amaral et al. [40] reported the similar observations that the first crack growth presenting a titled crack plane occurs when the load is still below the maximum and it is followed by cusps formation and coalescence. They stated that the mode II critical SERR obtained at the point where the microcracks ahead of the main crack tip coalesce overestimates the resistance at the onset of delamination. Therefore, in the present work, the moment when this tilted crack plane occurred was defined as the initiation point. In this respect, more guidance about determining crack initiation is needed in the testing standards. A high resolution at the crack tip during the image acquisition process is needed to further precisely specify this crack initiation angle (i.e. orientation of the titled crack plane) considering the resolution approximately in terms of 25–34 pixels/mm in the present work for ELS and MMB tests. Besides, the applicability of these test standards on very thick laminated pultruded composite plates should be schematically investigated further, as specimen thickness in the present work is close to recommended values.

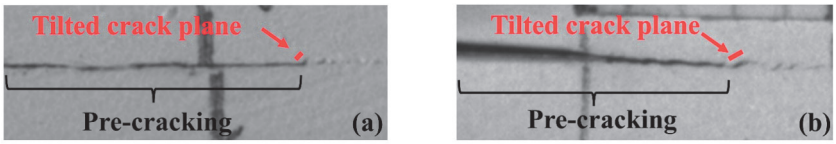

Fig. 14. The tilted crack plane ahead of the pre-crack tip observed during mode II ELS test (a) and mixed-mode I/II MMB test at the mode mix 0.67 (b).

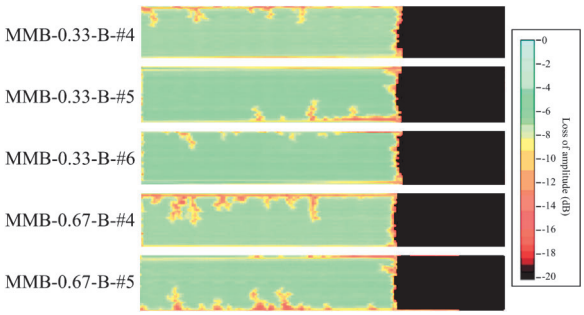

Fig. 15. C-scan results of MMB specimens with defects.

4.3. *Effect of defects on the fracture behaviour*

For the MMB tests, specimens from Panel B presented significant defects as shown in Fig. 15. Results from Fig. 9(a) and Fig. 10(a) show that for G_{II}/G_T=0.33 the specimens with defects fractured in a more brittle way, as compared to most of the defect-free specimens. Among the three defect-free specimens cut from Panel C, MMB-0.33-C-#1 presented relatively less stable crack propagation than MMB-0.33-C-#2 and MMB-0.33-C-#3, which might be attributed to the earlier detachment of loading blocks that terminated the test earlier. However, the critical SERR using the VIS method showed similar results for both specimens with and without defects (Table A6). This phenomenon suggests that defects mainly affect crack propagation, rather than crack initiation, for the mode-I dominate fracture behaviour. When increasing the mode mix ratio to 0.67, crack initiation seems to be delayed by the presence of defects, as a larger displacement and a larger critical SERR are presented at VIS (Fig. 9(b), Fig. 10(b), and Table A7). Meanwhile, crack propagation for specimens with defects was performed in a stable manner, which is similar to the defect-free specimens. The R-curves (Fig. 10(b)) suggest that higher energy may be consumed for crack propagation in the same length for specimens with defects. This phenomenon indicates that defects could act as barriers to shield the crack front and trigger new micro-crack generation, in line with the results reported by Li et al. [21,22]. Therefore, either detrimental or beneficial effects on the fracture behaviour of laminated pultruded composite plates can be created by manufacturing-induced defects, depending on the crack opening mode. Further investigations are needed to quantify the critical transition regarding the crack opening mode between detrimental and beneficial effect of defects, to determine if they can be well-arranged in a controllable way to improve the interlaminar crack resistance for laminated pultruded composites.

5. Conclusions

Based on DCB, ELS, and MMB test configurations, the interlaminar crack propagation for laminated pultruded composite plates was observed at four mode mix ratios. Together with microscopic inspection of fracture surfaces, the fracture behaviour of such bonded composite plates was characterised, while B-K law and power law were compared regarding their prediction of the mixed-mode I/II crack initiation toughness. In the meantime, the applicability of existing testing standards and the effect of manufacturing-induced defects on fracture properties were explored. The main conclusions are listed hereafter:

1) Stick-slip behaviour was observed for mode-I crack propagation, resulting in brittle failure in a few steps. Conversely, mode II crack propagation provides more stability in crack propagation along with the dominance of cohesive failure. For mixed-mode I/II fracture tests, fracture behaviour follows the mixture ratio, with stability towards cohesive failure during the crack growth observed for higher shear mode contribution.
2) Both the B-K and power law criteria are capable to describe the mixed-mode failure envelope at interfaces of laminated-pultruded plates. The fits using the power law suggest a linear relation between the mixed-mode I/II fracture toughness components could exist at interfaces of laminated pultruded plates.
3) The existing ISO/ASTM, DCB, ELS and MMB test standards provide sufficient support for characterising interlaminar fracture properties of laminated pultruded plates, even though their thickness slightly exceeds the recommended values. However, more guidance should be provided on visual observation of crack initiation, while further investigations are required to check applicability for very thick laminated pultruded composite plates.
4) For mixed-mode I/II fracture tests, manufacturing-induced defects can reduce fracture propagation toughness and cause more brittle behaviour in mode I dominant cases while toughening the interface in mode II dominant cases.

The present results support the use of existing standards to characterise laminated pultruded composite plates. This also suggests that common research practices for fatigue delamination growth tests, which are based on the quasi-static standards, can also be applied to laminated pultruded plates. Finally, a more detailed examination of the effect of the manufacturing defects on the fracture behaviour could suggest ways to increase the interfacial toughness of such plates.

CRediT authorship contribution statement

Xi Li: Writing – review & editing, Writing – original draft, Visualization, Validation, Software, Methodology, Investigation, Formal analysis, Data curation, Conceptualization. **Francisco Monticeli:** Writing – review & editing, Visualization, Validation, Methodology, Investigation, Formal analysis, Conceptualization. **John-Alan Pascoe:** Writing – review & editing, Supervision, Resources, Project administration, Methodology, Investigation, Funding acquisition, Formal analysis, Conceptualization. **Yasmine Mosleh:** Writing – review & editing, Supervision, Resources, Project administration, Methodology, Investigation, Funding acquisition, Formal analysis, Conceptualization.

Declaration of competing interest

The authors declare that they have no known competing financial interests or personal relationships that could have appeared to influence the work reported in this paper.

Data availability

Data will be available through the Zenodo community for D-STANDART: https://zenodo.org/communities/d-standart/records?q=&l=list&p=1&s=10&sort=newest.

Acknowledgements

The authors would like to acknowledge Dr. Jaykarna Bhangale for help in manufacturing the specimens and Dr. Ran Tao for help in the adhesive bonding of loading blocks. Thanks are given to technicians in DASM Lab at TU Delft for instructions and trainings of testing equipment. The research was funded by the European Union under GA No. 101091409 (D-STANDART). Views and opinions expressed are however those of the author(s) only and do not necessarily reflect those of the European Union. Neither the European Union nor the granting authority can be held responsible for them.

Appendix

Table A1
Fitting parameters involved in three different data reduction methods for each DCB specimen.

Specimen ID	Δ (mm)	n (log(mm/N)/ log(mm))	A^1 ((N/mm)$^{1/3}$)
DCB-A-#1	−7.31	2.76	32.54
DCB-A-#2	−31.77	2.39	43.65
DCB-A-#3	0.18	3.00	35.66
Mean	−12.97	2.72	37.28
Standard deviation	16.71	0.31	5.73

Table A2
Fitting parameter m and flexural modulus E_1 involved in three different data reduction methods for each ELS specimen.

Specimen ID	m (1/(N×mm^2))	E_1 (MPa)
ELS-A-#3	2.53E-8	1.82E+5
ELS-A-#4	2.51E-8	1.77E+5
ELS-A-#5	2.96E-8	2.05E+5
ELS-C-#6	2.43E-8	1.77E+5
ELS-C-#7	2.69E-8	1.83E+5
Mean	2.62E-8	1.85E+5
Standard deviation	2.10E-9	11627.55

Table A3
Bending modulus E_{1f} involved in the calculation of total energy release rate for each MMB specimen.

Mixed mode ratio: 0.33		Mixed mode ratio: 0.67	
Specimen ID	E_{1f} (MPa)	Specimen ID	E_{1f} (MPa)
MMB-0.33-C-#1	1.25E+5	MMB-0.67-C-#1	1.21E+5
MMB-0.33-C-#2	1.20E+5	MMB-0.67-C-#2	1.18E+5
MMB-0.33-C-#3	1.17E+5	MMB-0.67-C-#3	1.24E+5
MMB-0.33-B-#1	1.10E+5	MMB-0.67-B-#1	1.20E+5
MMB-0.33-B-#2	1.11E+5	MMB-0.67-B-#2	1.19E+5
MMB-0.33-B-#3	1.21E+5	–	–
Mean (Panel C)	1.21E+5	Mean (Panel C)	1.21E+5
Mean (Panel B)	1.14E+5	Mean (Panel B)	1.20E+5
Standard deviation (Panel C)	4041.45	Standard deviation (Panel C)	3000
Standard deviation (Panel B)	6082.76	Standard deviation (Panel B)	707.11

Table A4
Critical strain energy release rate G_{IC} at the initiation point (i.e. NL, 5 %/max and VIS) calculated by three different data reduction methods under pure mode-I. (Unit: J/m^2).

Specimen ID	NL			5 %/max			VIS		
	MBT	CC	MCC	MBT	CC	MCC	MBT	CC	MCC
DCB-A-#1	700	700	820	1000	850	1130	1020	1020	1170
DCB-A-#2	410	430	440	780	610	820	820	870	870
DCB-A-#3	700	700	700	960	840	940	990	990	960
Mean	600	610	650	910	770	960	940	960	1000
Standard deviation	167	156	194	117	136	156	108	79	154

Table A5
Critical strain energy release rate G_{IIC} at the initiation point (i.e. NL, 5 %/max and VIS) calculated by three different data reduction methods under pure mode-II. (Unit: J/m^2).

Specimen ID	NL			5 %/max			VIS		
	ECM	SBT	CBTE	ECM	SBT	CBTE	ECM	SBT	CBTE
ELS-A-#1	420	240	370	1670	970	1610	2670	1550	2750
ELS-A-#2	460	280	470	2480	1460	2710	2240	1350	2420
ELS-A-#3	320	160	280	1380	690	1290	2420	1210	2410
ELS-C-#4	330	200	310	2700	1630	2710	2810	1750	2830
ELS-C-#5	330	180	290	1420	790	1380	3030	1710	3190
Mean	370	210	340	1930	1110	1940	2640	1520	2720
Standard deviation	5.77	20	15.28	750.82	516.27	795.13	308.92	300.89	390.38

Table A6
Mode-I component G_I, mode-II component G_{II}, and total critical strain energy release rate G_T at the initiation point (i.e. NL, 5 %/max and VIS) under the mixed-mode ratio of 0.33 for MMB specimens with and without defects. (Unit: J/m^2).

Specimen ID	NL			5 %/max			VIS		
	G_I	G_{II}	G_T	G_I	G_{II}	G_T	G_I	G_{II}	G_T
MMB-0.33-C-#1	450	220	670	950	470	1420	930	460	1390
MMB-0.33-C-#2	380	190	570	930	460	1390	680	340	1020
MMB-0.33-C-#3	490	240	730	960	470	1430	870	430	1300
MMB-0.33-B-#1	730	360	1090	1040	510	1550	960	470	1430
MMB-0.33-B-#2	620	310	930	750	370	1120	820	400	1220
MMB-0.33-B-#3	520	260	780	850	420	1270	930	460	1390
Mean (Panel C)	440	220	660	950	470	1410	830	410	1240
Mean (Panel B)	620	310	930	880	430	1310	900	440	1350
Standard deviation (Panel C)	56	25	81	15	6	21	131	62	193
Standard deviation (Panel B)	105	50	155	147	71	218	74	38	111

Table A7
Mode-I component G_I, mode-II component G_{II}, and total critical strain energy release rate G_T at the initiation point (i.e. NL, 5 %/max and VIS) under the mixed-mode ratio 0.67 for MMB specimens with and without defects. (Unit: J/m^2).

Specimen ID	NL			5 %/max			VIS		
	G_I	G_{II}	G_T	G_I	G_{II}	G_T	G_I	G_{II}	G_T
MMB-0.67-C-#1	520	1020	1540	770	1530	2300	630	1240	1870
MMB-0.67-C-#2	440	870	1310	730	1440	2170	430	840	1270
MMB-0.67-C-#3	500	1000	1500	780	1540	2320	570	1130	1700
MMB-0.67-B-#1	480	930	1410	860	1670	2530	760	1480	2240
MMB-0.67-B-#2	440	880	1320	870	1730	2600	920	1840	2760
Mean (Panel C)	490	960	1450	760	1500	2260	540	1070	1610
Mean (Panel B)	460	910	1370	870	1700	2570	840	1660	2500
Standard deviation (Panel C)	42	81	123	26	55	81	103	207	309
Standard deviation (Panel B)	28	35	64	7	42	49	113	255	368

References

[1] Ennis BL, Das S, Norris RE. Economic competitiveness of pultruded fiber composites for wind turbine applications. Compos Part B Eng 2023;265. https://doi.org/10.1016/j.compositesb.2023.110960.
[2] Mindermann P, Witt MU, Gresser GT. Pultrusion-winding: A novel fabrication method for coreless wound fiber-reinforced thermoset composites with distinct cross-section. Compos Part A Appl Sci Manuf 2022;154:1–9. https://doi.org/10.1016/j.compositesa.2021.106763.
[3] Miller DA, Samborsky DD, Ennis BL. Mechanical Testing Summary: Optimized Carbon Fiber Composites in Wind Turbine Blade Design. 2019.
[4] Shang X, Marques EAS, Machado JJM, Carbas RJC, Jiang D, da Silva LFM. Review on techniques to improve the strength of adhesive joints with composite adherends. Compos Part B Eng 2019;177:107363. https://doi.org/10.1016/j.compositesb.2019.107363.
[5] Ma D, Verleysen P, Chandran S, Giglio M, Manes A. A modified peridynamic method to model the fracture behaviour of nanocomposites. Eng Fract Mech 2021;247:107614. https://doi.org/10.1016/j.engfracmech.2021.107614.
[6] ASTM D5528.. Standard test method for mode I interlaminar fracture toughness of unidirectional fiber-reinforced polymer matrix composites. ASTM Int 2014;03:1–12.
[7] ISO 15114. Fibre-reinforced plastic composites - Determination of the mode II fracture resistance for unidirectionally reinforced materials using the calibrated end-loaded split (C-ELS) test and an effective crack length approach 2014.
[8] ASTM D7905. Standard test method for determination of the mode II interlaminar fracture toughness of unidirectional fiber-reinforced polymer matrix composites. ASTM Int 2014;1–18. https://doi.org/10.1520/D7905.
[9] ASTM D6671/D6671M −22. Standard Test Method for Mixed Mode I-Mode II Interlaminar Fracture Toughness of Unidirectional Fiber Reinforced Polymer Matrix Composites. ASTM Int 2022:15.
[10] Sarrado C, Turon A, Costa J, Renart J. On the validity of linear elastic fracture mechanics methods to measure the fracture toughness of adhesive joints. Int J Solids Struct 2016;81:110–6. https://doi.org/10.1016/j.ijsolstr.2015.11.016.
[11] Lopes Fernandes R, Teixeira de Freitas S, Budzik MK, Poulis JA, Benedictus R. From thin to extra-thick adhesive layer thicknesses: Fracture of bonded joints under mode I loading conditions. Eng Fract Mech 2019;218. https://doi.org/10.1016/j.engfracmech.2019.106607.
[12] Cintra GG, Vieira JD, Cardoso DCT, Keller T. Mode I and Mode II fracture behavior in pultruded glass fiber-polymer – Experimental and numerical investigation. Compos Part B Eng 2023;266:110988. https://doi.org/10.1016/j.compositesb.2023.110988.
[13] Burda I, Brunner AJ, Barbezat M. Mode I fracture testing of pultruded glass fiber reinforced epoxy rods: Test development and influence of precracking method and manufacturing. Eng Fract Mech 2015;149:287–97. https://doi.org/10.1016/j.engfracmech.2015.08.009.
[14] Yan X, Guo X, Gao Y, Lin Y, Zhang N, Zhao Q. Mode-II fracture toughness and crack propagation of pultruded carbon Fiber-Epoxy composites. Eng Fract Mech 2023;279:109042. https://doi.org/10.1016/j.engfracmech.2022.109042.
[15] Zhang Y, Vassilopoulos AP, Keller T. Mode I and II fracture behavior of adhesively-bonded pultruded composite joints. Eng Fract Mech 2010;77:128–43. https://doi.org/10.1016/j.engfracmech.2009.09.015.
[16] Jiang Z, Fang Z, Yan L, Wan S, Fang Y. Mixed-mode I/II fracture criteria for adhesively-bonded pultruded GFRP/steel joint. Compos Struct 2021;255:113012. https://doi.org/10.1016/j.compstruct.2020.113012.
[17] Synytska A, Michel S, Pleul D, Bellmann C, Schinner R, Eichhorn K. Monitoring the surface tension of reactive epoxy-amine systems under different environmental conditions. J Adhension 2004;80:667–83. https://doi.org/10.1080/00218460490477639.
[18] Kumar RS. Effects of randomly distributed defects on Mode-I interlaminar fracture of composite materials. Eng Fract Mech 2021;248:107699. https://doi.org/10.1016/j.engfracmech.2021.107699.
[19] Kumar RS. Mode-II interlaminar fracture of composite materials in the presence of randomly distributed defects. Int J Fract 2021;231:201–21. https://doi.org/10.1007/s10704-021-00581-4.
[20] Ranade SR, Guan Y, Moore RB, Dillard JG, Batra RC, Dillard DA. Characterizing fracture performance and the interaction of propagating cracks with locally weakened interfaces in adhesive joints. Int J Adhes Adhes 2018;82:196–205. https://doi.org/10.1016/j.ijadhadh.2017.12.006.
[21] Li X, Tao R, Alfano M, Lubineau G. How variability in interfacial properties results in tougher bonded composite joints by triggering bridging. Int J Solids Struct 2020;191–192:87–98. https://doi.org/10.1016/j.ijsolstr.2019.11.021.
[22] Li X, Tao R, Yudhanto A, Lubineau G. How the spatial correlation in adhesion properties influences the performance of secondary bonding of laminated composites. Int J Solids Struct 2020;196–197:41–52. https://doi.org/10.1016/j.ijsolstr.2020.04.012.
[23] Zoltek. Zoltek PX35 Pultrusion n.d. https://doi.org/https://zoltek.com/datasheets/.
[24] Pérez-Galmés M, Renart J, Sarrado C, Costa J. Suitable specimen dimensions for the determination of mode II fracture toughness of bonded joints by means of the ELS test. Eng Fract Mech 2018;202:350–62. https://doi.org/10.1016/j.engfracmech.2018.07.039.
[25] Chudnovsky A. Slow crack growth, its modeling and crack-layer approach: A review. Int J Eng Sci 2014;83:6–41. https://doi.org/10.1016/j.ijengsci.2014.05.015.
[26] Floros IS, Tserpes KI, Löbel T. Mode-I, mode-II and mixed-mode I+II fracture behavior of composite bonded joints: Experimental characterization and numerical simulation. Compos Part B Eng 2015;78:459–68. https://doi.org/10.1016/j.compositesb.2015.04.006.
[27] Guo S, Xia Y, Wei X, Zhou Q. Investigation on the stable and stick-slip crack propagation behaviors in double cantilever beam test. J Adhes 2020;96:1198–218. https://doi.org/10.1080/00218464.2019.1568248.

[28] Ashcroft IA, Hughes DJ, Shaw SJ. Mode I fracture of epoxy bonded composite joints: 1. Quasi-static loading Int J Adhes Adhes 2001;21:87–99. https://doi.org/10.1016/S0143-7496(00)00038-5.
[29] Omairey S, Jayasree N, Kazilas M. Defects and uncertainties of adhesively bonded composite joints. SN Appl Sci 2021;3. https://doi.org/10.1007/s42452-021-04753-8.
[30] Xu W, Wei Y. Strength and interface failure mechanism of adhesive joints. Int J Adhes Adhes 2012;34:80–92. https://doi.org/10.1016/j.ijadhadh.2011.12.004.
[31] Pérez-Galmés M, Renart J, Sarrado C, Rodríguez-Bellido A, Costa J. A data reduction method based on the J-integral to obtain the interlaminar fracture toughness in a mode II end-loaded split (ELS) test. Compos Part A Appl Sci Manuf 2016;90:670–7. https://doi.org/10.1016/j.compositesa.2016.08.020.
[32] Nakar E, Ando S, Drug A, Toward IR. Studies on effect of pre-crack length variation on Inter-laminar fracture toughness of a Glass Epoxy laminated composite Studies on effect of pre-crack length variation on Inter- laminar fracture toughness of a Glass Epoxy laminated composite. IOP Conf. Ser. Mater Sci Eng 2016:012161. https://doi.org/10.1088/1757-899X/149/1/012161.
[33] Gupta S, West G, Wilson MA, Grutzik SJ, Warner DH. Identifying crack tip position and stress intensity factors from displacement data. Int J Fract 2023;243:47–63. https://doi.org/10.1007/s10704-023-00729-4.
[34] Orell O, Jokinen J, Kanerva M. Use of DIC in the characterisation of mode II crack propagation in adhesive fatigue testing. Int J Adhes Adhes 2023;122. https://doi.org/10.1016/j.ijadhadh.2023.103332.
[35] de Paula Santos LF, Monticeli FM, Ribeiro B, Costa ML, Alderliesten R, Botelho EC. Does carbon nanotube buckypaper affect mode-I and II interlaminar fracture toughness under quasi-static loading? Compos Struct 2023;323. https://doi.org/10.1016/j.compstruct.2023.117507.
[36] Rogers C, Greenhalgh ES, Robinson P. Developing a Mode II Fracture Model for Composite Laminates. 13th Eur Conf Compos Mater. 2014.
[37] Simon I, Banks-Sills L. Mixed mode I/II interlaminar initiation fracture toughness of a secondary bonded pultrusion composite laminate. Theor Appl Fract Mech 2021;114:103018. https://doi.org/10.1016/j.tafmec.2021.103018.
[38] Shahverdi M, Vassilopoulos AP, Keller T. Mixed-mode quasi-static failure criteria for adhesively-bonded pultruded GFRP joints. Compos Part A Appl Sci Manuf 2014;59:45–56. https://doi.org/10.1016/j.compositesa.2013.12.007.
[39] Brunner AJ. Experimental aspects of Mode I and Mode II fracture toughness testing of fibre-reinforced polymer-matrix composites. Comput Methods Appl Mech Eng 2000;185:161–72. https://doi.org/10.1016/S0045-7825(99)00257-1.
[40] Amaral L, Alderliesten R, Benedictus R. Towards a physics-based relationship for crack growth under different loading modes. Eng Fract Mech 2018;195:222–41. https://doi.org/10.1016/j.engfracmech.2018.04.017.